

AIAA-98-0786

Unsteady Simulations of Compressible Spatial Mixing Layers

C. Nelson*

Sverdrup Technology, Inc.

AEDC Group

Arnold Air Force Base, TN 37389-6001

S. Menon†

School of Aerospace Engineering

Georgia Institute of Technology

Atlanta, GA 30332-0150

1 Abstract

A local dynamic one-equation subgrid model has been used to carry out large-eddy simulations of unsteady spatially developing compressible mixing layers. Simulations of the supersonic mixing layers studied by Samimy and Elliott^{1,2} have been carried out. Despite the very high Reynolds numbers of these flows and the comparatively coarse grids employed, good qualitative and reasonable quantitative results are obtained.

2 Introduction

It has long been noted that turbulent compressible mixing layers grow slower than equivalent incompressible layers. Birch and Eggars³ believed that it was due to the mean density gradient. Later work⁴⁻⁶ showed that the primary cause of the reduced growth rate was linked to compressibility.

Several ideas have been presented to account for this decrease in growth rate. Papamoschou⁷ suggested that this was due to eddy shocklets: regions of strong compression caused by the turbulent motion which would increase energy dissipation. This increased energy dissipation has been associated with the dilatation dissipation term in the Reynolds averaged turbulent kinetic energy equation. Zeman⁸ and Sarkar *et al.*⁹ developed models for the dilatation dissipation term which were added to standard k - ϵ models. These models were able to better predict the reduction in mixing layer growth rate associated with increased compressibility.

A similar term exists in the LES subgrid kinetic energy equation. For LES, however, very little work on dilatation dissipation has been conducted. Spyropoulos and Blaisdell¹⁰ claimed no such modifications were needed for their dynamic algebraic model, since it apparently adjusted automatically to account for compressibility effects. Their

work, however, did not investigate strongly compressible flows. Therefore, the limitations of the dynamic model, if any, were not thoroughly tested.

The importance of eddy shocklets was called into question by Sandham and Reynolds¹¹ who were unable to find any such structures in 3-*D* DNS of temporal mixing layers. They suggested, rather, that linear stability theory accounted for most of the observed decrease in mixing layer growth rates.¹² Linear theory predicted the increase in three dimensionality of mixing layers as convective Mach number increases. This was found to be due to oblique instability modes becoming dominant at high compressibility, whereas purely two dimensional modes dominate at lower convective Mach numbers. This is in keeping with experimental observations.¹³⁻¹⁶

Sarkar *et al.*⁹ also attributed some of the kinetic energy growth rate reduction to the action of pressure-dilatation, and derived a model for this term for Reynolds averaged Navier-Stokes (RANS) solvers. A related term occurs in the subgrid kinetic energy equation. The work by Koutmos *et al.*¹⁷ used a model proposed by Schumann to address this issue in an LES context. For compressible decaying isotropic turbulence, however, pressure-dilatation's contribution to dissipation was found to be insignificant.¹⁸

A third mechanism proposed for the observed reduction in kinetic energy growth rates is the reduction in Reynolds shear stress anisotropy. This reduction results in decreased turbulent energy production.¹⁹ Sarkar has found in direct simulations of homogeneous shear flow that the reduction in kinetic energy growth is primarily due to this reduced level of energy production, not any explicitly dilatational effects.^{20,21} While pressure-dilatation and dilatation-dissipation were found to increase with compressibility, they did not add appreciably to the overall dissipation.

The inability of conventional RANS based codes to capture the decrease in growth rate led to the development of the models for dilatation dissipation. The inherent weaknesses in the RANS approach, however, make general development and application difficult. In this paper, the LES technique is applied to study spatially evolving

*Senior Engineer, Member AIAA

†Professor, Senior Member AIAA

Copyright © 1998 by C. Nelson and S. Menon- Published by the American Institute of Aeronautics and Astronautics, Inc. with permission.

mixing layers. In LES, all scales larger than the grid scale are captured using a time- and space-accurate numerical scheme, and only the small scales are modeled. The present approach uses a localized dynamic model for the subgrid kinetic energy. It is the purpose of this paper to demonstrate that the LES technique can be used to capture the effects of compressibility without any model adjustments.

3 Governing Equations

The equations of motion for LES are obtained by filtering the Navier-Stokes equations. For compressible flow, the standard technique is to use a Favre (or density weighted) filter. This avoids some complexity, but gives rise to difficulties when comparing to experimental data, which is not Favre filtered. Thus, here we explicitly include the compressibility effects into the model by using standard (not mass weighted) spatial filtering. Written this way, the governing equations may be written as:

$$\frac{\partial \bar{\rho}}{\partial t} = -\frac{\partial \bar{\rho} \bar{u}_i}{\partial x_i} - \frac{\partial}{\partial x_i} (\overline{\rho u_i} - \bar{\rho} \bar{u}_i) \quad (1)$$

$$\begin{aligned} \frac{\partial \bar{\rho} \bar{u}_i}{\partial t} &= -\frac{\partial}{\partial x_j} (\overline{\rho u_i u_j}) - \frac{\partial \bar{\rho}}{\partial x_i} + \frac{\partial \bar{t}_{ij}}{\partial x_j} \\ &\quad - \frac{\partial}{\partial x_j} (\overline{\rho u_i u_j} - \bar{\rho} \bar{u}_i \bar{u}_j) + \frac{\partial}{\partial x_j} (\bar{\tau}_{ij} - \bar{t}_{ij}) \\ &\quad - \frac{\partial}{\partial t} (\overline{\rho u_i} - \bar{\rho} \bar{u}_i) \end{aligned} \quad (2)$$

$$\begin{aligned} \frac{\partial \bar{\rho} \bar{E}}{\partial t} &= -\frac{\partial}{\partial x_i} (\bar{\rho} \bar{E} + \bar{p}) \bar{u}_i - \frac{\partial}{\partial x_i} (\overline{\rho E u_i} - \bar{\rho} \bar{E} \bar{u}_i) \\ &\quad - \frac{\partial}{\partial x_i} (\overline{\rho u_i} - \bar{\rho} \bar{u}_i) \\ &\quad + \frac{\partial}{\partial x_i} (\bar{u}_j \bar{t}_{ij}) + \frac{\partial}{\partial x_i} (\overline{u_j \tau_{ij}} - \bar{u}_j \bar{t}_{ij}) \\ &\quad + \frac{\partial}{\partial x_i} \left(\bar{\kappa} \frac{\partial \bar{T}}{\partial x_i} \right) + \frac{\partial}{\partial x_i} \left(\overline{\kappa \frac{\partial T}{\partial x_i}} - \bar{\kappa} \frac{\partial \bar{T}}{\partial x_i} \right) \\ &\quad - \frac{R}{\gamma - 1} \frac{\partial}{\partial t} (\overline{\rho T} - \bar{\rho} \bar{T}) - \frac{1}{2} \frac{\partial}{\partial t} (\overline{\rho u_i u_i} - \bar{\rho} \bar{u}_i \bar{u}_i) \\ &\quad + \frac{\partial}{\partial t} (\bar{\rho} k^{sgs}) \end{aligned} \quad (3)$$

The resolved viscous stress tensor in the above equation takes the following form:

$$\bar{t}_{ij} = 2\bar{\mu} \left[\frac{1}{2} \left(\frac{\partial \bar{u}_i}{\partial x_j} + \frac{\partial \bar{u}_j}{\partial x_i} \right) - \frac{1}{3} \frac{\partial \bar{u}_k}{\partial x_k} \delta_{ij} \right] \quad (4)$$

Viscosity is assumed to follow Sutherland's Law (using the filtered temperature as the argument). The other viscous term in the above equation, $\bar{\tau}_{ij}$, is the filter of the exact viscous stress tensor. The total energy is defined here as:

$$\bar{E} = \bar{e} + \frac{1}{2} \bar{u}_i \bar{u}_i + k^{sgs} \quad (5)$$

The subgrid kinetic energy (k^{sgs}) is defined as:

$$k^{sgs} = \frac{1}{2} (\overline{u_i u_i} - \bar{u}_i \bar{u}_i) \quad (6)$$

The subgrid kinetic energy is allowed to evolve according to its own transport equation, as described in the following section. The LES thermal conductivity ($\bar{\kappa}$) and internal energy (\bar{e}) are, like viscosity, assumed to be functions of the filtered temperature. Finally, the LES equation of state is written as:

$$\bar{p} = \bar{\rho} R \bar{T} + R (\overline{\rho T} - \bar{\rho} \bar{T}) \quad (7)$$

4 Closure of Subgrid Terms

Many of the subgrid terms in the above equations have been found to be generally small (in compressible homogeneous isotropic flow²²), and therefore they have been neglected. These include the viscous subgrid terms ($(\bar{\tau}_{ij} - \bar{t}_{ij})$ and $(\overline{u_j \tau_{ij}} - \bar{u}_j \bar{t}_{ij})$), the state equation subgrid term ($R (\overline{\rho T} - \bar{\rho} \bar{T})$), and the subgrid heat convection term ($\overline{\kappa \frac{\partial T}{\partial x_i}} - \bar{\kappa} \frac{\partial \bar{T}}{\partial x_i}$).

The density-velocity correlation term which appears in the LES continuity equation (1) is a purely compressible term which has no direct analog in constant density flows. Some properties, however, can be deduced *a priori*. First, this subgrid term may be rewritten as the difference between the Favre filtered and "straight filtered" velocity:

$$c_i^{sgs} = \overline{\rho u_i} - \bar{\rho} \bar{u}_i = \bar{\rho} (\tilde{u} - \bar{u}) \quad (8)$$

Obviously, since this term appears only in the compressible equations, any model for it should vanish for a constant density flow. Also, this term is expected to be significant only in regions of strong compression, such as a shock. This is in keeping with the findings of Chen *et al.*,²³ who investigated the differences between Favre filtering and conventional filtering in the context of RANS simulations of combustion. They found that the differences between \tilde{u} and \bar{u} were virtually undetectable in regions with mild density gradients. When density is varying more abruptly, it can be argued, in a fashion similar to that used for the mixing length model of turbulent heat flux,²⁴ that the contribution of this term should be proportional to the mean density gradient.

In light of this, a gradient diffusion model is adopted for this term:

$$c_i^{sgs} = \overline{\rho u_i} - \bar{\rho} \bar{u}_i \approx -\nu_c \frac{\partial \bar{\rho}}{\partial x_i} \quad (9)$$

The scaling factor in the above equation (ν_c - designated the "compressibility viscosity") is formulated in the following manner. Since this term is expected to be significant only near strong density (pressure) gradients, a switch is used to prevent excessive dissipation from being added to regions where the mean flow is smooth. It is

defined in a discrete sense in a manner similar to that developed by MacCormack and Baldwin.²⁵ On the i -faces, for example, it may be written:

$$S_{p_{i+\frac{1}{2},j,k}} = \max(S_{p_{i,j,k}}, S_{p_{i+1,j,k}}) \quad (10a)$$

$$\text{where } S_{p_{i,j,k}} = \frac{|p_{i+1,j,k} - 2p_{i,j,k} + p_{i-1,j,k}|}{p_{i+1,j,k} + 2p_{i,j,k} + p_{i-1,j,k}} \quad (10b)$$

A characteristic length and velocity can be used to obtain the correct dimensions for this term. The grid spacing, Δ , is chosen as the length scale. The characteristic velocity is defined as the magnitude of the velocity normal to the cell face. Thus the expression for the “compressibility viscosity” may be written as:

$$\nu_c = a_c S_p |\bar{u}_k n_k| \Delta \quad (11)$$

where a_c is a scaling parameter chosen as:

$$a_c = \begin{cases} a_0 \exp\left[\frac{-1}{K_1(R_{e\Delta} - R_{e\min})}\right] & R_{e\Delta} > R_{e\min} \\ 0 & R_{e\Delta} \leq R_{e\min} \end{cases} \quad (12)$$

$$R_{e\Delta} = \frac{|\bar{u}_k n_k| \Delta}{\nu + \nu_t}$$

Numerical experiments on the one-dimensional nonlinear Burger’s equation have been used to obtain the above form for the scaling factor. The Burger’s equation was used as a model problem to test the behavior of the numerical scheme (with an added dissipation term similar to the proposed model) in the presence of sharp gradients, such as those found at shocks. The exact solution (a hyperbolic tangent) is compared to the numerically obtained solution to find an optimal value for the scaling factor for different cell “Reynolds” numbers. A curve fit is applied to the resulting data to obtain an analytic expression for the scaling factor (at a cell face): The value used for K_1 is 0.257, and the minimum cell Reynolds number is 1.67. A value of 0.60 was used for the scaling coefficient, a_c , in this work. The denominator of the above expression for cell Reynolds number includes an eddy viscosity (ν_t), which is defined as:

$$\nu_t = c_\nu \sqrt{k^{sgs}} \Delta \quad (13)$$

The eddy viscosity is used in modeling the “incompressible” portions of the subgrid terms for the momentum, energy, and subgrid kinetic energy equations. In the momentum equation, the “incompressible” portion of the subgrid stress tensor is modeled as:

$$\begin{aligned} \tau_{ij}^{sgs(i)} &= \bar{\rho} (\overline{u_i u_j} - \bar{u}_i \bar{u}_j) \\ &\approx -2\bar{\rho} \nu_t \left(\bar{S}_{ij} - \frac{1}{3} \bar{S}_{kk} \delta_{ij} \right) + \frac{2}{3} \bar{\rho} k^{sgs} \delta_{ij} \end{aligned} \quad (14)$$

In the energy equation, the pressure-velocity correlation and convective subgrid terms are combined by rewriting

them in terms of total enthalpy and modeled as:

$$\bar{\rho} (\overline{H u_i} - \bar{H} \bar{u}_i) \approx -c_e \bar{\rho} \sqrt{k^{sgs}} \Delta \frac{\partial \bar{H}}{\partial x_i} \quad (15)$$

Finally, in the subgrid kinetic energy equation, the transport of k^{sgs} by subgrid processes is modeled as:

$$\text{Subgrid Transport} \approx \frac{\partial}{\partial x_i} \left(\bar{\rho} \nu_t \frac{\partial k^{sgs}}{\partial x_i} \right) \quad (16)$$

The “compressibility” viscosity ν_c is used to model additional effects of compressibility in the momentum, energy, and subgrid kinetic energy equations (using simple gradient diffusion models). Incorporating the above models and assumptions into the governing equations results in the following model LES equations:

$$\frac{\partial \bar{\rho}}{\partial t} = -\frac{\partial \bar{\rho} \bar{u}_i}{\partial x_i} + \frac{\partial}{\partial x_i} \left(\nu_c \frac{\partial \bar{\rho}}{\partial x_i} \right) \quad (17)$$

$$\begin{aligned} \frac{\partial \bar{\rho} \bar{u}_i}{\partial t} &= -\frac{\partial}{\partial x_j} (\bar{\rho} \bar{u}_i \bar{u}_j) - \frac{\partial \bar{p}}{\partial x_i} + \frac{\partial \bar{t}_{ij}}{\partial x_j} - \frac{\partial \tau_{ij}^{sgs(i)}}{\partial x_j} \\ &\quad - \frac{\partial M_{ij}^{sgs(c)}}{\partial x_j} \end{aligned} \quad (18)$$

$$\begin{aligned} \frac{\partial \bar{\rho} \bar{E}}{\partial t} &= -\frac{\partial}{\partial x_i} (\bar{\rho} \bar{E} + \bar{p}) \bar{u}_i + \frac{\partial}{\partial x_i} \left(c_e \bar{\rho} \sqrt{k^{sgs}} \Delta \frac{\partial \bar{H}}{\partial x_i} \right) \\ &\quad + \frac{\partial}{\partial x_i} (\bar{u}_j \bar{t}_{ij}) + \frac{\partial}{\partial x_i} \left(\left[\bar{\kappa} + \frac{\gamma c_v \bar{\rho} \nu_c}{Pr} \right] \frac{\partial \bar{T}}{\partial x_i} \right) \end{aligned} \quad (19)$$

$$\begin{aligned} \frac{\partial \bar{\rho} k^{sgs}}{\partial t} &= -\frac{\partial}{\partial x_i} (\bar{\rho} k^{sgs} \bar{u}_i) + \frac{\partial}{\partial x_i} \left(\bar{\rho} (\nu_t + \nu_c) \frac{\partial k^{sgs}}{\partial x_i} \right) \\ &\quad - \tau_{ij}^{sgs(i)} \frac{\partial \bar{u}_j}{\partial x_i} - \bar{\rho} c_\epsilon \frac{(k^{sgs})^{\frac{3}{2}}}{\Delta} \end{aligned} \quad (20)$$

$$\bar{p} = \bar{\rho} R \bar{T} \quad (21)$$

where

$$M_{ij}^{sgs(c)} = -2\bar{\rho} \nu_c \left(\bar{S}_{ij} - \frac{1}{3} \bar{S}_{kk} \delta_{ij} \right) \quad (22)$$

The above equations contain three model coefficients (c_ν , c_ϵ , and c_e). These coefficients are computed dynamically for this study. In order to do this, it is assumed that the subgrid scales behave very much like the smallest resolved scales. This proposition has been experimentally shown to be reasonable for the subgrid stress tensor by Liu, *et al.*²⁶ for the case of free jets. A “test” filter is used to isolate the smallest resolved scales. This filter (denoted by a circumflex- *e.g.* $\widehat{\phi}$) must have a characteristic length, $\widehat{\Delta}$, larger than the grid resolution. Usually $\widehat{\Delta}$ is taken to be twice the size of the local grid spacing (Δ), but this is somewhat arbitrary. Coefficients may then be computed by comparing quantities that are resolved in the LES flow field but not by a corresponding “test” filtered field.

Because only positive filters are used in this work, the incompressible portion of the subgrid stress tensor

$(\tau_{ij}^{sgs(i)})$ must be positive semidefinite. Therefore, the model coefficient, c_ν , is constrained such that the resulting modelled tensor has this property. The conditions which enforce this are known as the “realizability” conditions.²⁷ These may be stated as follows:

$$\tau_{\alpha\alpha}^{sgs(i)} \geq 0 \text{ for } \alpha \in \{1, 2, 3\} \quad (23a)$$

$$\left| \tau_{\alpha\beta}^{sgs(i)} \right|^2 \leq \tau_{\alpha\alpha}^{sgs(i)} \tau_{\beta\beta}^{sgs(i)} \text{ for } \alpha, \beta \in \{1, 2, 3\} \quad (23b)$$

$$\det \left(\tau_{ij}^{sgs(i)} \right) \geq 0 \quad (23c)$$

Note that, unlike conventional tensor notation, repeated indices in the above expressions do not indicate summation. In addition, c_ν is also constrained such that the resulting effective viscosity ($\nu + \nu_t$) is positive. The other two constants (c_ε and c_e) are also constrained to be positive.

The subgrid stress tensor model coefficient is found using the following equation:

$$c_\nu = \frac{-L_{ij} D_{ij}}{2D_{ij} D_{ij}} \quad (24)$$

where:

$$L_{ij} = \widehat{\rho} \left(\widehat{u_i u_j} - \widehat{u_i} \widehat{u_j} \right) - \frac{1}{3} \widehat{\rho} \left(\widehat{u_k u_k} - \widehat{u_k} \widehat{u_k} \right) \delta_{ij} \quad (25)$$

$$D_{ij} = \widehat{\Delta} \widehat{\rho} \left(\frac{\widehat{u_k u_k}}{2} - \widehat{u_k} \widehat{u_k} \right)^{\frac{1}{2}} \left(\widehat{S}_{ij} - \frac{\widehat{S}_{kk}}{3} \delta_{ij} \right) \quad (26)$$

$$\widehat{S}_{ij} = \frac{1}{2} \left[\frac{\partial \widehat{u}_i}{\partial x_j} + \frac{\partial \widehat{u}_j}{\partial x_i} \right] \quad (27)$$

The dissipation model coefficient is computed as:

$$c_\varepsilon = \frac{\widehat{\Delta} \left(\widehat{\overline{t}_{ij}} \frac{\partial \widehat{u}_i}{\partial x_j} - \widehat{T}_{ij} \frac{\partial \widehat{u}_i}{\partial x_j} \right)}{\widehat{\rho} \left(\frac{\widehat{u_k u_k}}{2} - \widehat{u_k} \widehat{u_k} \right)^{\frac{3}{2}}} \quad (28)$$

where the viscous stresses resolved on the test filtered field are defined as:

$$\widehat{T}_{ij} = \widehat{\mu} \left(\frac{\partial \widehat{u}_i}{\partial x_j} + \frac{\partial \widehat{u}_j}{\partial x_i} - \frac{2}{3} \frac{\partial \widehat{u}_k}{\partial x_k} \delta_{ij} \right) \quad (29)$$

The energy equation model coefficient is computed as follows:

$$c_e = \frac{n_i d_i}{d_i d_i} \quad (30)$$

$$\text{where } n_i = \widehat{\rho} \left(\widehat{H} \widehat{u}_i - \widehat{H} \widehat{u}_i \right) \quad (31)$$

$$d_i = \widehat{\rho} \left(\frac{\widehat{u_k u_k}}{2} - \widehat{u_k} \widehat{u_k} \right)^{\frac{1}{2}} \widehat{\Delta} \frac{\partial \widehat{H}}{\partial x_i} \quad (32)$$

The above model differs from the original compressible extension²⁸ of Germano’s dynamic model²⁹ in that, rather than being completely algebraic, the current work uses the subgrid kinetic energy, which develops with the rest of the flow field, as the basis for deriving the velocity scale used to compute the eddy viscosity. The subgrid kinetic energy acts as a limiter on the eddy viscosity, eliminating much of the instability which, in previous dynamic models, necessitated *ad hoc* averaging in one or more homogeneous directions. Any remaining instability is controlled through the enforcement of the conditions (*e.g.* realizability) discussed above.

5 Numerical Algorithm

The choice of numerical algorithm is extremely important when attempting to perform time-accurate simulations of turbulent flows. Schemes which give excellent results for other applications, are often unacceptable due to excessive numerical dissipation. An example of this is shown in figure 1. In this plot, three different schemes are employed to simulate the same homogeneous isotropic turbulent flow on a coarse grid, but without any subgrid model. The three schemes are the Gottlieb-Turkel³⁰ extension of the MacCormack scheme (GT 2-4), a fifth order upwind-biased, Advection Upstream Splitting Method (AUSM) scheme,³¹ and a new scheme (New 2-4) which, like GT 2-4, is a higher order extension to MacCormack’s scheme. The experimental results are from Comte-Bellot and Corrsin’s grid turbulence tests.³² Without a model, the 2-4 schemes show significantly less energy decay than the experiment predicted, but the AUSM scheme, because of its much higher level of numerical dissipation, obtains results which mimic the experiment.

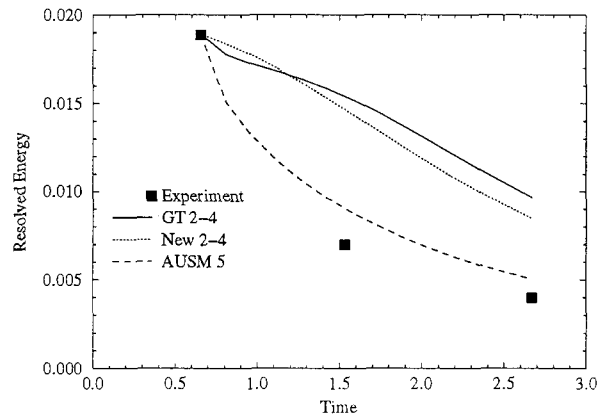


Figure 1: Comparison of predicted kinetic energy decay for various numerical schemes

If one could rely on the numerical scheme’s dissipation to damp the resolved energy at the correct rate, then subgrid models would be unnecessary. Unfortunately, there

are no guarantees that this will take place. In this case, for example, while the resolved energy is being dissipated as the solution progresses, AUSM's results do not match the experiment. Thus a subgrid model is still necessary. If the cell Reynolds number can be kept low enough, the effects of numerical dissipation will remain sufficiently small that the subgrid model can still function. The Reynolds number for this case, for instance, while high enough to make DNS difficult, is still comparatively low, and the numerical dissipation has not exceeded the actual dissipation observed in the experiment. For a truly high Reynolds number flow, however, it is easy to see that the dissipation in the AUSM scheme would overwhelm the viscous and turbulent forces to the extent that no subgrid model could compensate enough to obtain the correct results.

The numerical scheme used for this work is a MacCormack-type method similar to the Gottlieb-Turkel method.³⁰ In contrast to that method, the current scheme is truly fourth order in space (on a uniform grid) and (like Gottlieb-Turkel) it is second order in time. The algorithm is implemented in a finite volume sense. On stretched grids, the algorithm uses an interpolant which attempts to preserve some of the properties that the scheme has on uniform grids, but the scheme does not remain strictly fourth order.

6 Model Validation

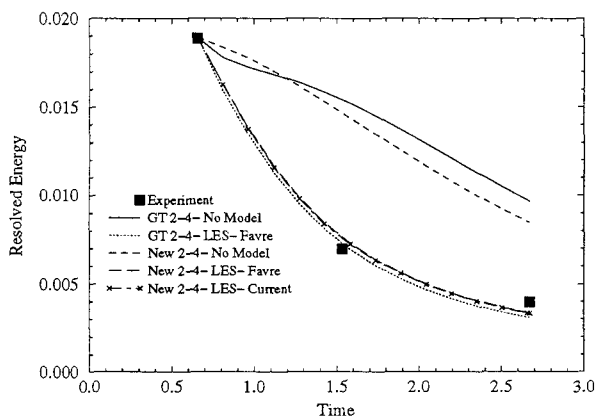


Figure 2: Resolved kinetic energy of isotropic LES compared with grid turbulence experimental data

Several decaying isotropic cases have been run to validate the numerical scheme and the model. The first case to be considered here attempts to duplicate the grid-turbulence experiments of Comte-Bellot and Corrsin.³² Figure 2 shows the results (on the same 32^3 grid) from two different schemes (Gottlieb-Turkel's 2-4 and the current 2-4) and different modelling strategies (no model, the conventional Favre filtering approach, and the current approach). As

can be seen, the two numerical schemes give very similar results. Also, without a model, the energy decay is not properly captured. Finally, in the near-incompressible regime, it is seen that the Favre filtering approach and the current approach to subgrid modelling yield the same results. This is to be expected, since the difference between a Favre filter and a 'straight' filter is solely dependant on density variations.

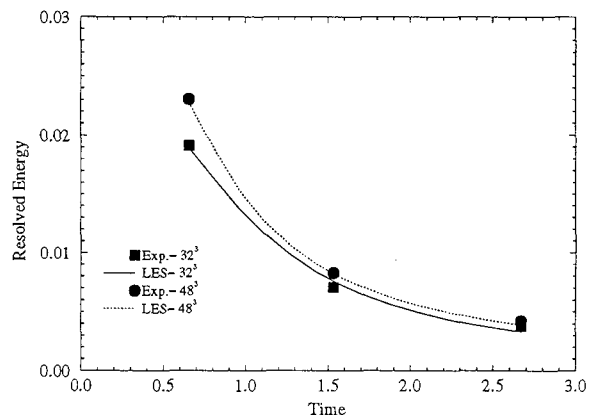


Figure 3: Comparison of the resolved kinetic energy from LES with the filtered experimental data

Two grid resolutions were run (32^3 and 48^3). The decay of the mean resolved kinetic energy is plotted in figure 3. It should be noted that, for a direct simulation, a grid of on the order of 384^3 points would be needed. Even with the fairly coarse 32^3 grid, the model predicts reasonable agreement with the experimental data. Naturally, the 48^3 case is in even better agreement. These results are consistent with those of other researchers^{10, 33, 34} and demonstrate the validity of the model in the near-incompressible regime.

To examine the behavior of the model in a more compressible regime, LES results (on a 16^3 grid) from a decaying isotropic case are compared with filtered DNS results (on a 64^3 grid) for the same case. The initial turbulent Mach number for the DNS was 0.826, and the initial Taylor Reynolds number was 34.9. Again, the code obtains good results, as shown in figures 4 (mean Mach number), 5 (resolved kinetic energy normalized by the experimentally measured initial kinetic energy), and 6 (RMS of density fluctuations normalized by the mean density).

7 The Mixing Layer Simulations

Isotropic turbulence cases, such as those discussed above, can be useful in model development, but the real challenge for LES lies in applying it to problems of a more practical nature. As a step in that direction, spatially evolving mixing layers were studied. The simulated mixing layers were designed to duplicate the experimental

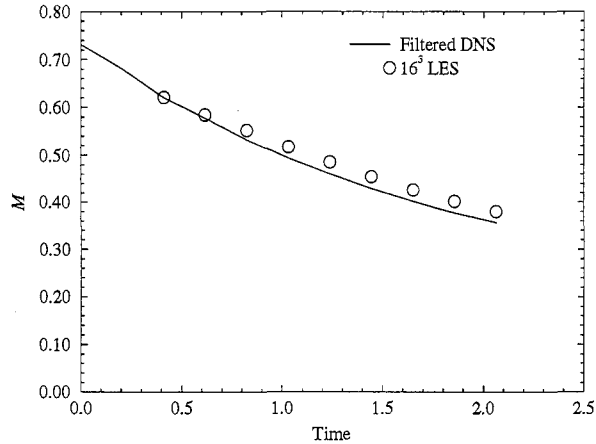


Figure 4: Evolution of the mean Mach number in compressible decaying isotropic turbulence

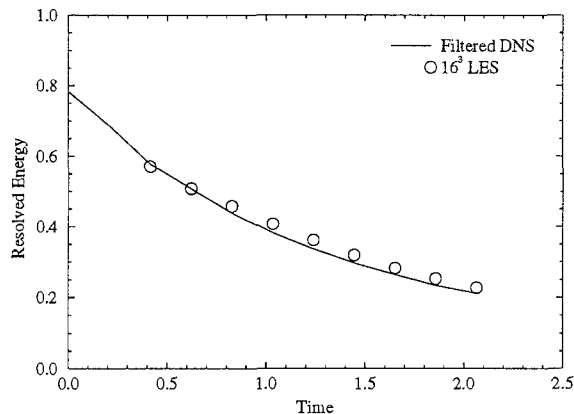


Figure 5: Decay of mean resolved kinetic energy in compressible decaying isotropic turbulence

work of Samimy and Elliott. The incoming flow parameters for these two cases are summarized in Table 1. Here, M_c is the convective Mach number.⁵ The Reynolds number for both of these cases is on the order of one million per meter.

7.1 Computational Domain

The domain used for the simulations of both cases (shown schematically in figure 7) starts just upstream of the splitter plate lip, and ends 0.4 meters downstream of the lip. Since experimental data is only available for the first 250 mm, this allows a sufficient buffer to prevent corruption of the solution from the outflow boundary. As in the experiments, the splitter plate is 0.5 mm thick at the lip. In the experimental rig, the subsonic side of the splitter plate was machined at approximately a 1° angle. This

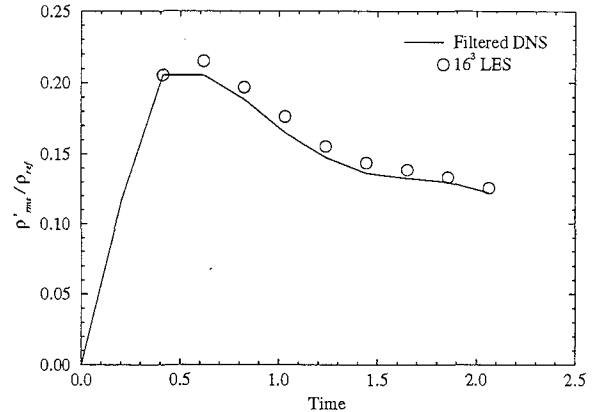


Figure 6: Normalized RMS of density fluctuations in compressible decaying isotropic turbulence

Case	T_0 (K)	P_{01} (kPa)	M_1	M_2	M_c
1	291.0	314.0	1.80	0.51	0.53
2	276.0	722.0	3.01	0.45	0.88

Case	U_1 (m/s)	$\frac{U_2}{U_1}$	$\frac{\rho_2}{\rho_1}$	δ (mm)
1	479.5	0.355	0.638	8.0
2	597.7	0.246	0.370	9.2

Table 1: Flow parameters for spatial mixing layer cases

is ignored, however, for the LES, and the subsonic side of the splitter plate is assumed to be aligned horizontally. The full height of the experimental rig (152.4 mm) is simulated, but only the middle 76 mm (out of 152 mm) are computed in the spanwise direction.

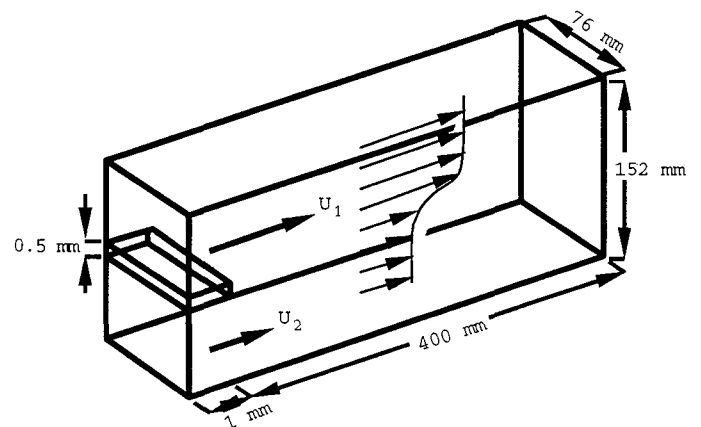


Figure 7: Spatial mixing layer computational domain schematic

The grids employed for this case had a curvilinear H - H topology. Three different grids were used in order to investigate the effects of resolution: $61 \times 41 \times 18$, $91 \times 61 \times 34$, and $121 \times 91 \times 50$ (including ghost points). Of these, the two higher resolution grids gave essentially the same

solution (although, by definition, true grid independence will never be obtained in an LES).²² Only the results from the highest resolution grid are presented here.

7.2 Boundary Conditions

The upper and lower boundaries are treated as slip-walls, since the grid does not have adequate resolution to resolve the boundary layers. Periodic boundary conditions were used in the spanwise direction. This was done for convenience rather than any requirement of the code or the subgrid models. The flow at the outflow boundary was computed after the manner of Thompson³⁵ and Poinso and Lele.³⁶ The inflow on the supersonic side is fully specified, while on the subsonic side, a characteristic boundary condition was employed. In order to better match the experimental predictions, pseudo-turbulent velocity fluctuations were added at the inflow boundaries.

Conceptually, the present approach to inflow turbulence may be described as computing a “box” of frozen turbulence which is convected by the mean flow into the computational domain. This field is computed initially in a cubic domain that is assumed periodic in all directions. For the sake of economy, it is computed on a 48^3 uniform Cartesian grid. Given the assumed spectrum (similar to Lee, Lele, and Moin³⁷), this level of resolution is sufficient to capture the majority of the energy containing wavenumbers, but it does mean that near the splitter plate, where grid points are highly concentrated, the computational domain is able to resolve much higher wavenumbers than are calculated in the inflow turbulence. For curvilinear grids, the velocity field must now be interpolated to a grid whose j - k planes (which are also y - z planes in the current spatial mixing layer case) match the actual inflow boundary grid and are uniformly spaced in the i direction (which is aligned with the x coordinate axis- the direction of mean flow). Here, the inflow boundary is vertical and is uniformly spaced in the k direction, so that a simple cubic spline along vertical grid lines is sufficient, but in other, more general, cases a two- or three-dimensional interpolating technique would be necessary.

One now has a solenoidal isotropic velocity field which has been computed on a grid which can be allowed to “convect” into the computational domain. This field, however, does not take into account the experimentally determined distribution of turbulence, nor does it take into account the varying distribution of resolved and unresolved turbulence due to differences in grid cell sizes. Thus, the velocity field must be modified, and a subgrid kinetic energy field computed such that the following relationship is satisfied:

$$\langle \overline{u'^2} \rangle_{ik} + \frac{2}{3} \langle k^{sgs} \rangle_{ik} = \sigma_u^2(y) \quad (33)$$

In the above equation, the angle brackets, $\langle \rangle_{ik}$, represent averaging in an i - k plane. Note that in a more general configuration, averaging would be performed only in

the i direction, since the grid might vary in the k direction. The other terms in the above equation are defined as follows: $\overline{u'}$ is the resolved inflow turbulence u -velocity field; k^{sgs} is the (yet to be determined) subgrid kinetic energy relative to the grid at the inflow boundary; and σ_u is the experimentally determined streamwise turbulent intensity (from Elliott² for the current work). In the absence of more complete information, the v and w components of velocity are assumed to behave in the same manner as u .

Given the assumed form of the energy spectrum and the grid resolution, an estimate can be made for the fraction of the turbulent energy which is resolved and how much energy is in the subgrid. Once the subgrid portion of the energy is known, the resolved turbulent velocity field which is entering the computational domain through the location in question can be scaled as follows:

$$\left(\overline{u'_i} \right)_{final} = \overline{u'_i} \sqrt{\frac{3(1 - E_{sgs})\sigma_u^2}{\langle \overline{u'_j u'_j} \rangle_{xz}}} \quad (34)$$

In the above expression, $\langle \overline{u'_j u'_j} \rangle_{xz}$ is the average (in the $x - z$ plane) of the unscaled inflow velocity perturbation field and E_{sgs} is the fraction of energy in the subgrid. One can also compute the average value of k_{sgs} which will enter the computational domain at this point:

$$k_{avg}^{sgs} = \frac{3E_{sgs}\sigma_u^2}{2} \quad (35)$$

This provides an estimate for the average amount of subgrid kinetic energy entering at any given point, but it does not provide any information about its specific spatial distribution. Several researchers (such as Liu *et al.*²⁶ and Meneveau³⁸) have found that the actual subgrid terms are similar to the highest wavenumber components of the resolved field. In keeping with this idea (and similar to the dynamic model coefficient calculations), the subgrid kinetic energy field is computed using the resolved field and a test field. This is then scaled to match the predicted value of the average subgrid kinetic energy from equation 36:

$$k^{sgs} = \left(\widehat{\overline{u'_i u'_i}} - \widehat{\overline{u'_i u'_i}} \right) \frac{k_{avg}^{sgs}}{\langle \widehat{\overline{u'_j u'_j}} - \widehat{\overline{u'_j u'_j}} \rangle_{xz}} \quad (36)$$

For the supersonic side of the mixing layer, the perturbation velocities are added to the mean quantities and the sum is directly specified at the inflow boundary. For the subsonic side, however, while the v and w components of velocity can be specified directly, the velocity perturbation in the streamwise direction is input as a perturbation in the total pressure and total temperature. This is found to work reasonably well, although this case is not really a

fair test, because the high speed side's perturbations are so much larger than the low speed side's that the latter are comparatively insignificant. Indeed, Samimy and Elliott have presented no data on the boundary layers or levels of turbulence for the low speed side inflow.

7.3 Results

The general procedure used for both the cases presented here was to run the solver until the initial conditions had been washed out of the domain. At this point (designated as a single flowthrough time), time averaging was begun. The simulations were then run for four ($M_c = 0.86$) or five ($M_c = 0.51$) more flowthrough times. By this time, the time-averaged statistics were essentially stationary. Despite the relative coarseness of even the finest grid used in this study ($121 \times 91 \times 50$), the results are surprisingly good when compared to experiment. The momentum thickness as a function of position downstream of the splitter plate, shown in figure 8, is reasonably well captured by the LES. The effect of compressibility is shown in the decrease in thickness (both in the simulation and experiment) for the higher convective Mach number case.

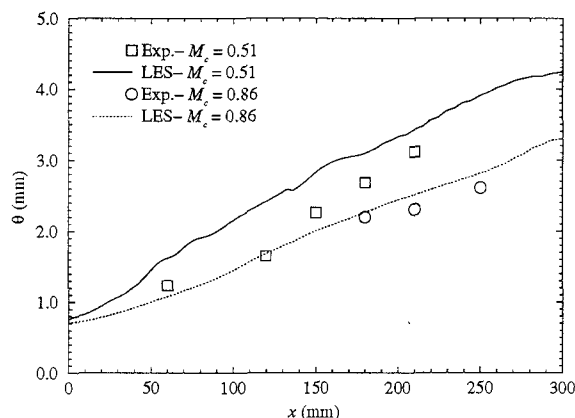


Figure 8: Comparison of LES predicted momentum thickness with the experimental data of Samimy and Elliott

In general, the simulation results for the $M_c = 0.51$ agree very well with experiment. Normalized velocity profiles for this case at various streamwise stations are plotted in figure 9. The agreement with the experimental data is excellent. As the figure shows, the self-similar character of the mean flow is well resolved by the current scheme.

Turbulent quantities are also in good agreement with experiment. Figure 10 shows streamwise turbulent intensity profiles at the same locations as for the previous figure. Both the peak magnitude and the overall distribution of turbulence are well predicted compared to the experiment. The width is correct, as is the shape and the self-similar nature of the profiles. Note, however, that

the freestream values are underpredicted (probably due to lack of resolution in these areas). As with the experiment, the U^* profiles showed self-similarity earlier than the turbulent quantities, which are not fully similar until 150mm downstream of the splitter plate. For the succeeding plots of turbulent quantities, data is shown only for those measuring stations which are downstream of the onset of self-similar behavior.

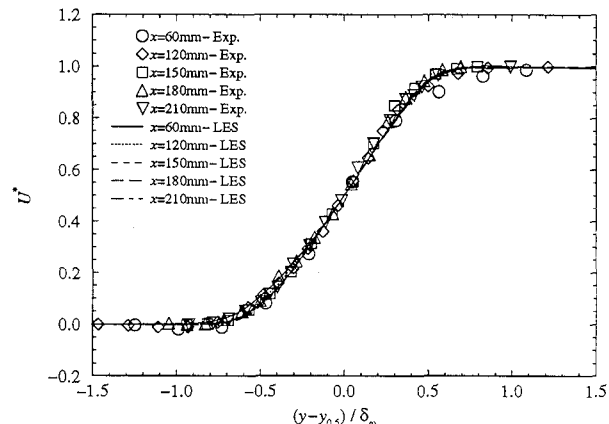


Figure 9: Normalized mean velocity profiles in the $M_c = 0.51$ mixing layer

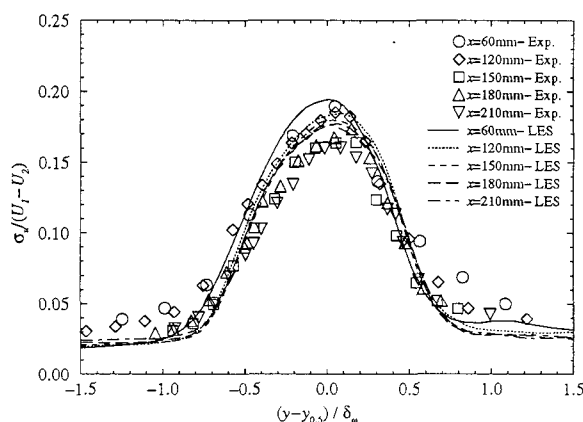


Figure 10: Profiles of streamwise turbulence intensity in the $M_c = 0.51$ mixing layer

The lateral turbulence intensity, shown in figure 11, is also in excellent agreement with experiment. Not only are the shape and the width of the profiles in the self-similar region correct, but the magnitude is also correct. The Reynolds stress profiles ($\overline{u'v'}$) shown in figure 12, are not as well resolved. Although the width of the profiles is correct and self-similar behavior is predicted, the magnitudes are significantly higher in the simulation. There are several possible sources for this error. It may be a result

of deficiencies in formulation of the current model. Errors in the numerical scheme (either dispersion or weaknesses in the scheme's ability to handle sharp curvature) might also play a part. Another possibility is a deficiency in the incoming pseudo-turbulence.

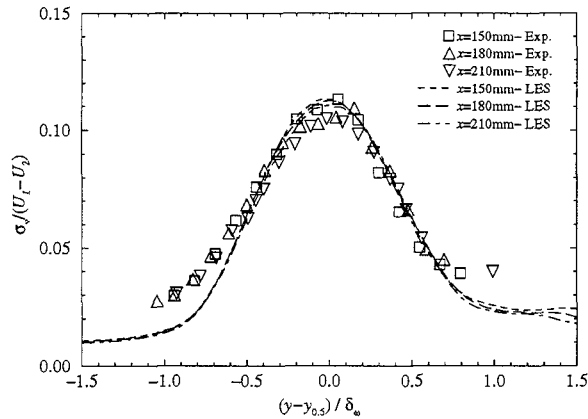


Figure 11: Profiles of lateral turbulence intensity in the $M_c = 0.51$ mixing layer

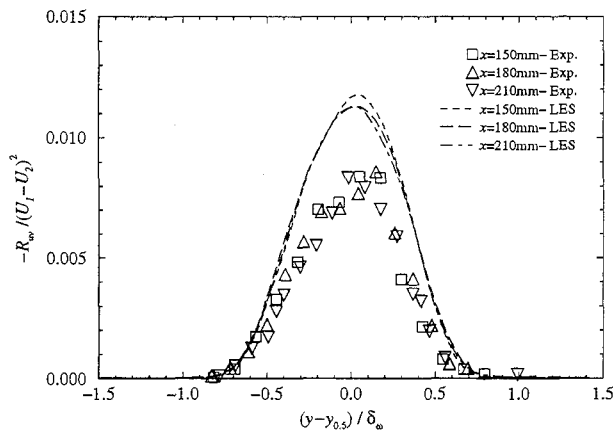


Figure 12: Reynolds stress profiles in the $M_c = 0.51$ mixing layer

The ability of the LES to capture the higher moments was also evaluated. Figures 13 and 14 show respectively, the streamwise and lateral turbulent transport of turbulent kinetic energy. It can be seen that these third order velocity fluctuation correlations are in excellent agreement with the measured data. Similarly, the streamwise and transverse velocity skewness are also well resolved for this case (see figures 15 and 16). Self-similarity is achieved, and the profiles show the correct shape and magnitude within the core region. The peak values, however, are slightly overpredicted. This is due to the previously discussed drop-off in the predicted turbulence in-

tensties away from the core region.

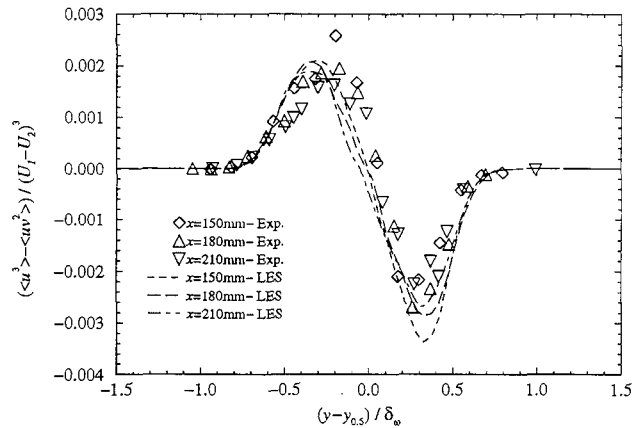


Figure 13: Streamwise turbulent energy transport in the $M_c = 0.51$ mixing layer

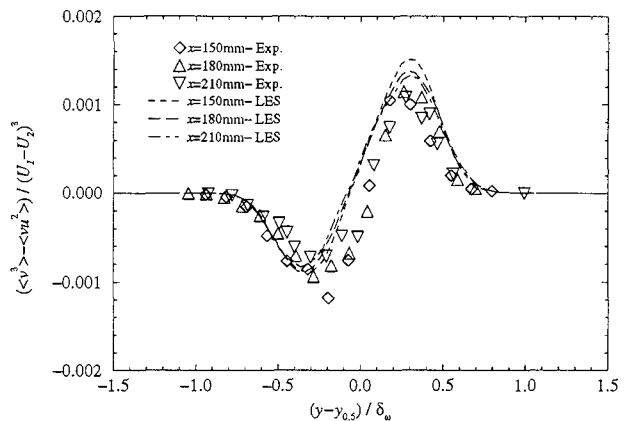


Figure 14: Lateral turbulent energy transport in the $M_c = 0.51$ mixing layer

The velocity flatness profiles (figure 17 and 18) also show very good agreement with experiment in the majority of the mixing layer. On the high speed side, however, the results become unstable above a non-dimensional coordinate of 0.5. Similar, though not as dramatic, instability is observed on the low-speed side for $(y - y_{0.5}) / \delta_w$ less than 1.0. The reasons for this behavior are the same as those cited above for the skewness: the underprediction of the turbulence intensity at the fringes of the mixing region.

The current model, therefore, has been quite successful in predicting the major features of a low to moderate compressibility mixing layer. Self-similarity is achieved in the core region of the mixing layer for all of the turbulent moments that were examined. Quantitative and qualitative agreement was obtained with experiment on all of

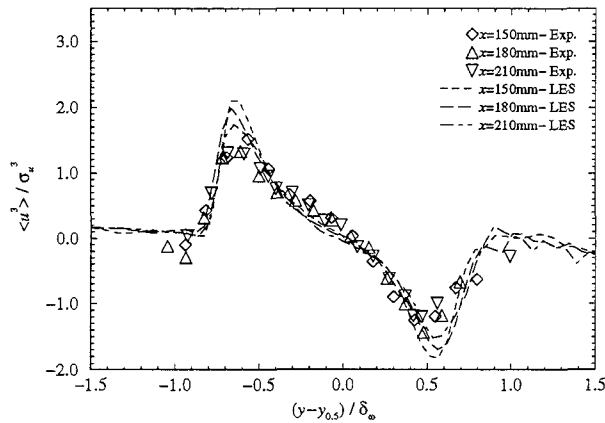


Figure 15: Streamwise velocity skewness profiles in the $M_c = 0.51$ mixing layer

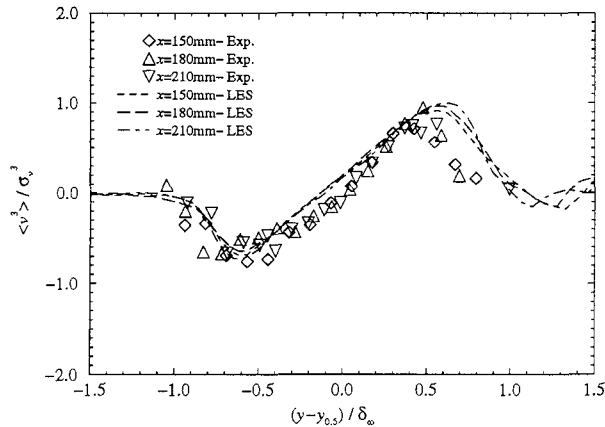


Figure 16: Lateral velocity skewness profiles in the $M_c = 0.51$ mixing layer

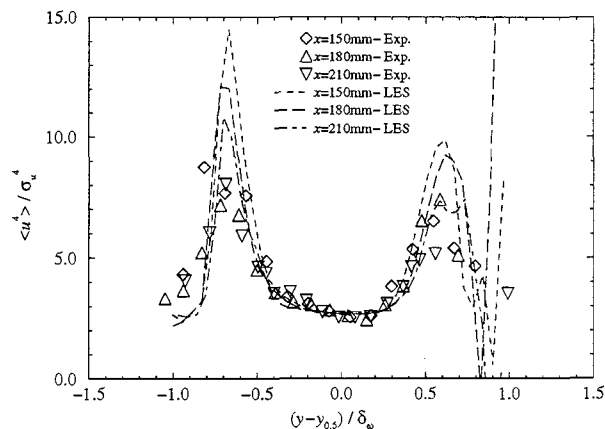


Figure 17: Streamwise velocity flatness profiles in the $M_c = 0.51$ mixing layer

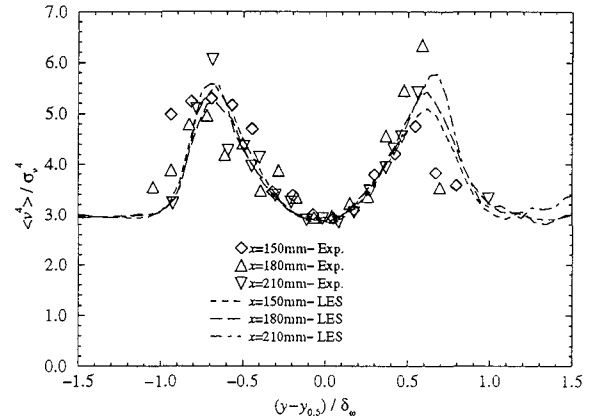


Figure 18: Lateral velocity flatness profiles in the $M_c = 0.51$ mixing layer

the quantities examined except the off-diagonal Reynolds stresses (R_{uv}), which were somewhat overpredicted.

In general, the results from simulations of the $M_c = 0.86$ mixing layer show more divergence from the experimental results than for the previous case. As mentioned above, these results are from flow fields which have been averaged (in time) over four flowthrough times. The normalized streamwise velocity profiles are shown in figure 19. Good agreement is obtained both in the shape and self-similar nature of the curves. Note that the horizontal axis coordinate for this case has been non-dimensionalized using the shear thickness rather than the vorticity thickness. This is because the vorticity thickness growth is predicted as being somewhat irregular for this case (unlike the $M_c = 0.51$ case). Thus, when this quantity is used as the normalizing factor, an artificial scattering is introduced. The shear thickness does not, in general, exhibit the same problem. In other respects, the results for this case were analyzed in the same manner as the $M_c = 0.51$ case.

Discrepancies between experiment and simulation become more apparent when turbulent quantities are examined. While the low-speed side of the curve is reasonably well predicted, the streamwise turbulence intensity profiles (shown in figure 20) are significantly overpredicted on the high-speed side. In general, the magnitude is also somewhat overpredicted. In addition, the width of the profile appears to be greater than in the experiments. The results are, however, self-similar. The self-similarity indicates that the problem is not growing spatially, but the dynamic model coefficients and ν_c may be similarly in error everywhere in the domain. One possible factor causing this is the use of a pressure switch in the computation of ν_c . A density switch might be more appropriate in this case, since the terms which are being modeled are directly related to density, and only indirectly to pressure. Unfortunately, the experimental data did not contain error

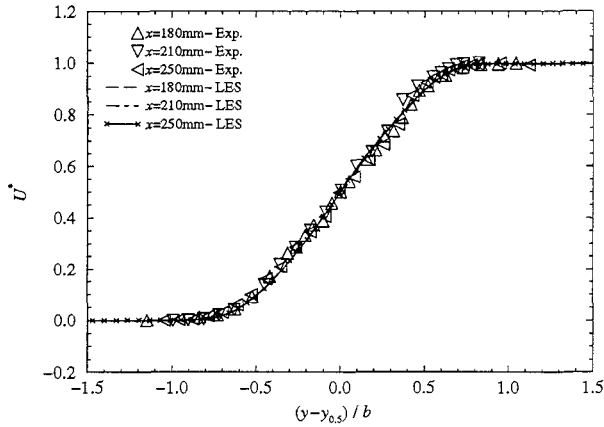


Figure 19: Normalized mean velocity profiles in the $M_c = 0.86$ mixing layer

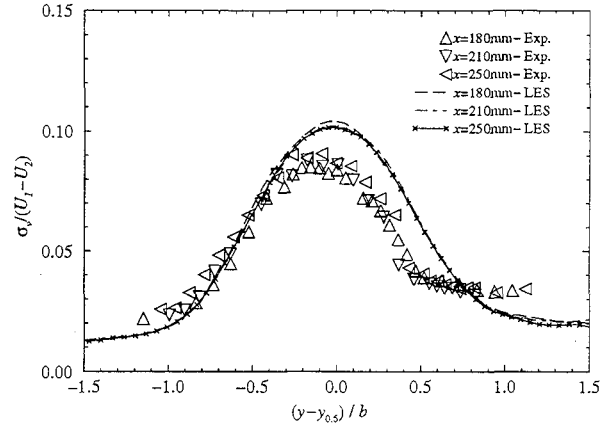


Figure 21: Profiles of lateral turbulence intensity in the $M_c = 0.86$ mixing layer

estimates, so it is impossible to say whether any part of the observed discrepancies might be due to experimental error.

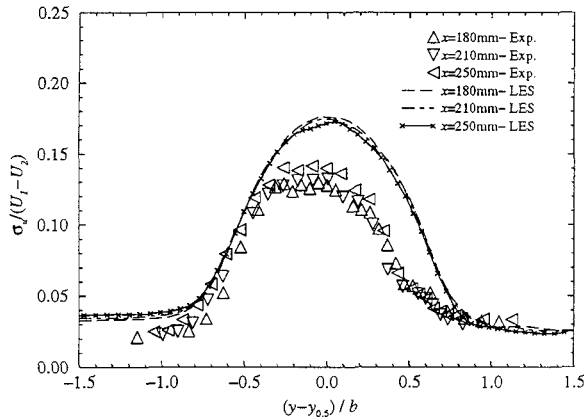


Figure 20: Profiles of streamwise turbulence intensity in the $M_c = 0.86$ mixing layer

This trend of reasonable predictions on the low-speed side and overprediction on the high speed side is seen on almost all of the turbulent quantities. The lateral turbulence intensity profiles, for example, are shown in figure 21. As before, they are somewhat skewed toward the high speed side of the flow, and the peak magnitude is overpredicted, though not as much as is the streamwise intensity. Again, the profiles are strongly self-similar.

The Reynolds stress profiles, shown in figure 22, are similarly skewed, but the magnitude is overpredicted to a greater degree than in the previous two plots. This is similar to the behavior that is observed in the $M_c = 0.51$ simulations, as shown above.

Third order correlations (figures 23 and 24) show a sim-

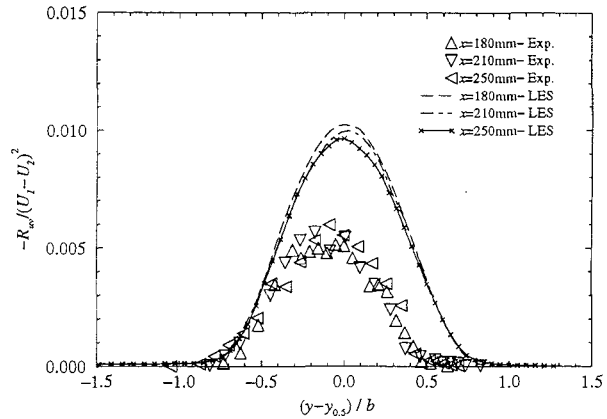


Figure 22: Reynolds stress profiles in the $M_c = 0.86$ mixing layer

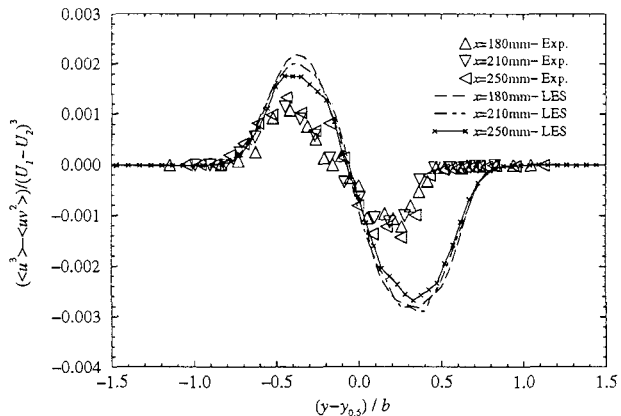


Figure 23: Profiles of streamwise turbulent transport of turbulent energy in the $M_c = 0.86$ mixing layer

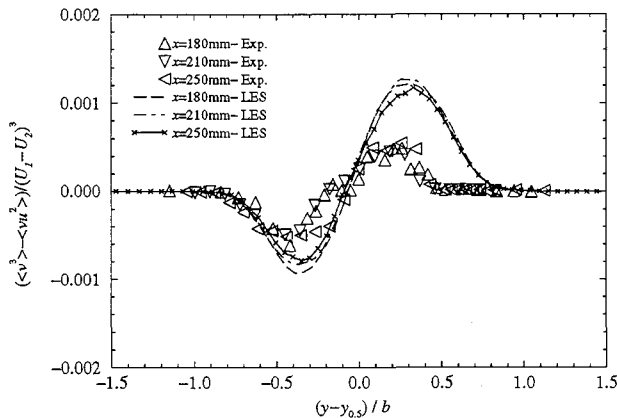


Figure 24: Profiles of lateral turbulent transport of turbulent energy in the $M_c = 0.86$ mixing layer

ilar trend of overpredicting the high-speed side and better agreement on the low-speed side. These are plots of the transport of turbulent kinetic energy by streamwise and lateral velocity fluctuations, respectively. Streamwise velocity skewness (figure 25) shows excellent agreement on the low-speed side of the mixing layer. Again, however, the high speed side of the mixing layer is not correctly predicted. Instead of the flattened character found in this region in the experiment, the profiles take the same general shape as was observed in the $M_c = 0.51$ mixing layer. The same basic trend is visible in the lateral velocity skewness, shown in figure 26. This quantity, however, is underpredicted on the low-speed side, in contrast to the previously mentioned quantities.

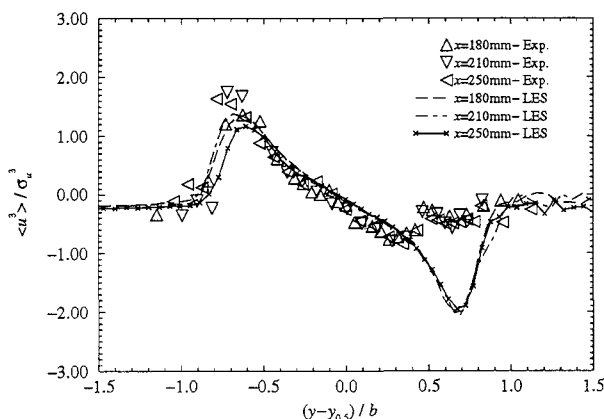


Figure 25: Streamwise velocity skewness profiles in the $M_c = 0.86$ mixing layer

The behavior of the velocity flatness (figures 27 and 28) is similar to the above skewness profiles. Again, the high-speed side is incorrectly predicted in much the same shape as for $M_c = 0.51$, while the low-speed side is in

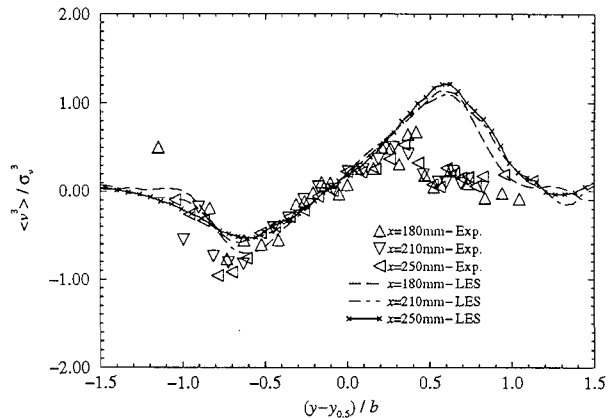


Figure 26: Profiles of lateral velocity skewness in the $M_c = 0.86$ mixing layer

reasonably good agreement with experiment. As with the lower Mach number case, the profiles become extremely unstable on the high-speed side beyond the edge of the mixing layer (non-dimensional coordinates greater than about 0.6) due to the drop-off in predicted turbulence intensity in that region.

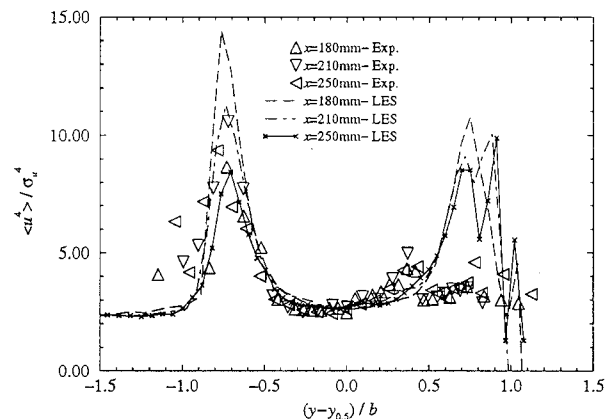


Figure 27: Profiles of streamwise velocity flatness in the $M_c = 0.86$ mixing layer

8 Conclusions

The current scheme, in combination with the compressible local dynamic subgrid model, has been shown to work reasonably well for turbulent flows with low to moderate compressibility- even when relatively coarse grids are used. In the decaying isotropic turbulence cases, the scheme closely matched experimental and DNS results. In the spatial mixing layer cases, the simulations compared extremely well with experiment for the lower convective

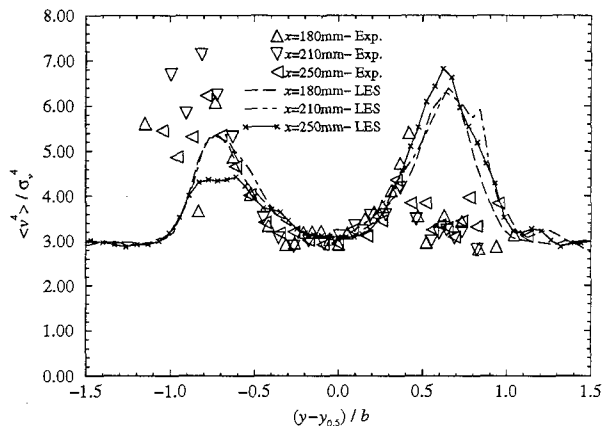


Figure 28: Lateral velocity flatness profiles in the $M_c = 0.86$ mixing layer

Mach number case. The higher convective Mach number case also captured the growth of the shear layer, as well as the expected self-similarity. Many of the expected qualitative features of the flow were also resolved.

It appears, however, that the model is not properly predicting a fundamental feature of highly compressible turbulence. Specifically, it is not capturing the full extent of the suppression of turbulence in the high speed region with increasing compressibility. This is illustrated in figure 29 which shows that the peak magnitudes of the streamwise and lateral turbulent intensities, as well as the Reynolds stress. While Elliott observed decreases in all three quantities, the current work predicts only a slight decrease in the streamwise intensity. Goebel and Dutton³⁹ (also see Gruber *et al.*⁴⁰) observed a trend similar to that of the present work: streamwise intensity remained roughly constant as Mach number increased. The behavior of the lateral intensity and Reynolds stress, however, does not agree with either set of experiments. While these values do decrease with increasing convective Mach number, they do not do so to the extent predicted by experiment.

Based on the above plots, it would seem that the majority of the error is from the high speed side of the mixing layer, rather than uniformly distributed throughout. From the experimental results, it appears that strong compressibility effects are felt strongly on the high speed side of the mixing layer, and these effects are not being correctly captured by the model. Thus, while the method appears to be adequate for low to moderate compressibility, the present results suggest that more research is needed to enhance the accuracy for highly compressible, high Reynolds number flows.

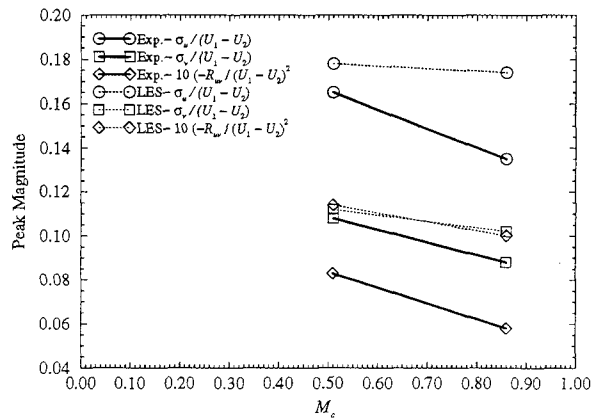


Figure 29: Maximum turbulence intensities and Reynolds stress versus convective Mach number

9 Acknowledgments

The authors would like to acknowledge the financial support of the Fluid Dynamics Division of the Office of Naval Research. Additional funding was also provided by the Air Force Office of Scientific Research under the Focused Research Initiative. Computer time was provided by the Aeronautical Systems Center at Wright-Patterson Air Force Base under the Department of Defense Major Shared Resource Center program. The authors would like to thank Prof. M. Samimy for providing the raw data from Dr. Elliott's experimental work.

References

- [1] M. Samimy, M. F. Reeder, and G. S. Elliott. Compressibility effects on large structures in free shear flows. *Physics of Fluids A*, 4(6):1251–1258, 1992.
- [2] G. Elliott. *A Study of Compressible Mixing Layers Using Laser Based Diagnostic Techniques*. PhD thesis, The Ohio State University, 1993.
- [3] S. F. Birch and J. M. Eggers. A critical review of the experimental data for developed free turbulent shear layers. In *Free Turbulent Shear Flows*, pages 11–37. NASA SP-321, 1972.
- [4] G. L. Brown and A. Roshko. On density effects and large structure in turbulent mixing layers. *Journal of Fluid Mechanics*, 64(4):775–816, 1974.
- [5] D. Papamoschou and A. Roshko. The compressible turbulent shear layer: an experimental study. *Journal of Fluid Mechanics*, 197:453–477, 1988.
- [6] D. W. Bogdanoff. Compressibility effects in turbulent shear layers. *AIAA Journal*, 21(6):926–927, 1983.

- [7] D. Papamoschou. Structure of the compressible turbulent shear layer. *AIAA Journal*, 29(5):680–681, 1991.
- [8] O. Zeman. Dilatation dissipation: The concept and application in modeling compressible mixing layers. *Physics of Fluids A*, 2(2):178–188, 1990.
- [9] S. Sarkar, G. Erlebacher, M. Y. Hussaini, and H. O. Kreiss. The analysis and modelling of dilatational terms in compressible turbulence. *Journal of Fluid Mechanics*, 227:473–493, 1991.
- [10] E. T. Spyropoulos and G. A. Blaisdell. Evaluation of the dynamic subgrid-scale model for large eddy simulations of compressible turbulence flows. *AIAA-95-0355*, 1995.
- [11] N. D. Sandham and W. C. Reynolds. Three-dimensional simulations of large eddies in the compressible mixing layer. *Journal of Fluid Mechanics*, 224:133–158, 1991.
- [12] N. D. Sandham and W. C. Reynolds. Compressible mixing layer: Linear theory and direct simulations. *AIAA Journal*, 28(4):618–624, 1990.
- [13] D. Papamoschou and A. Roshko. Observations of supersonic free shear layers. *AIAA-86-0162*, 1986.
- [14] N. T. Clemens and M. G. Mungal. Two- and three-dimensional effects in the supersonic mixing layer. *AIAA Journal*, 30(4):973–981, 1992.
- [15] N. L. Messersmith, S. G. Goebel, J. P. Renie, J. C. Dutton, and H. Krier. Investigation of supersonic mixing layers. *Journal of Propulsion and Power*, 6(4):353–354, 1990.
- [16] G. S. Elliott, M. Samimy, and S. A. Arnette. Study of compressible mixing layers using filtered Rayleigh scattering based visualizations. *AIAA Journal*, 30(10):2567–2569, 1992.
- [17] P. Koutmos, C. Mavridis, and D. Papailiou. A study of turbulent diffusion flames formed by planar fuel injection into the wake formation region of a slender square cylinder. In *Submitted to 26th International Symposium on Combustion*, 1996.
- [18] S. Lee, S. K. Lele, and P. Moin. Eddy shocklets in decaying compressible turbulence. *Physics of Fluids A*, 3(4):657–664, 1991.
- [19] S. Sarkar, G. Erlebacher, and M. Y. Hussaini. Compressible homogeneous shear: Simulation and modeling. Technical Report ICASE 92-6, Institute for Computer Applications in Science and Engineering, 1992.
- [20] S. Sarkar. The stabilizing influence of compressibility on turbulence in high-speed shear flows. *AIAA-94-2243*, 1994.
- [21] S. Sarkar. The stabilizing effect of compressibility in turbulent shear flow. *Journal of Fluid Mechanics*, 282:163–186, 1995.
- [22] C. C. Nelson. *Simulations of Spatially Evolving Compressible Turbulence Using a Local Dynamic Subgrid Model*. PhD thesis, Georgia Institute of Technology, 1997.
- [23] C. Chen, J. J. Riley, and P. A. McMurtry. A study of favre averaging in turbulent flows with chemical reaction. *Combustion and Flame*, 87:257–277, 1991.
- [24] H. Tennekes and J. L. Lumley. *A First Course in Turbulence*. The MIT Press, 1972.
- [25] R. W. MacCormack and B. S. Baldwin. A numerical method for solving the navier-stokes equations with application to shock-boundary layer interactions. *AIAA-75-1*, 1975.
- [26] S. Liu, C. Meneveau, and J. Katz. On the properties of similarity subgrid-scale models as deduced from measurements in a turbulent jet. *Journal of Fluid Mechanics*, 275:85–, 1994.
- [27] B. Vreman, B. Geurts, and H. Kuerten. Realizability conditions for the turbulent stress tensor in large-eddy simulation. *Journal of Fluid Mechanics*, 276:351–362, 1994.
- [28] P. Moin, K. Squires, W. Cabot, and S. Lee. A dynamic subgrid-scale model for compressible turbulence and scalar transport. *Physics of Fluids A*, 3(11):2746–2757, 1991.
- [29] M. Germano, U. Piomelli, P. Moin, and W. H. Cabot. A dynamic subgrid-scale eddy viscosity model. In *Center for Turbulence Research- Proceedings of the Summer Program 1990*, pages 5–17, 1990.
- [30] D. Gottlieb and E. Turkel. Dissipative two-four methods for time-dependant problems. *Mathematics of Computation*, 30(136):703–723, 1976.
- [31] M.-S. Liou and Jr. Steffen, C. J. A new flux splitting scheme. *Journal of Computational Physics*, 107:23–39, 1993.
- [32] G. Comte-Bellot and S. Corrsin. Simple Eulerian time correlation of full- and narrow-band velocity signals in grid-generated, 'isotropic' turbulence. *Journal of Fluid Mechanics*, 48(2):273–337, 1971.
- [33] W.-W. Kim. *A New Dynamic Subgrid-Scale Model for Large-Eddy Simulation of Turbulent Flows*. PhD thesis, Georgia Institute of Technology, 1996.
- [34] S. Ghosal, T. S. Lund, P. Moin, and K. Akselvoll. A dynamic localization model for large-eddy simulation of turbulent flows. *Journal of Fluid Mechanics*, 286:229–255, 1995.

- [35] K. W. Thompson. Time-dependant boundary conditions for hyperbolic systems, II. *Journal of Computational Physics*, 89:439–461, 1990.
- [36] T. J. Poinsot and S. K. Lele. Boundary conditions for direct simulations of compressible viscous flows. *Journal of Computational Fluids*, 101:104–129, 1992.
- [37] S. Lee, S. K. Lele, and P. Moin. Simulation of spatially evolving turbulence and the applicability of Taylor’s hypothesis in compressible flow. *Physics of Fluids A*, 4(7):1521–1530, 1992.
- [38] C. Meneveau. Statistics of turbulence subgrid-scale stresses: Necessary conditions and experimental tests. *Physics of Fluids*, 6(2):815–833, 1994.
- [39] S. G. Goebel and J. C. Dutton. Experimental study of compressible turbulent mixing layers. *AIAA Journal*, 29(4):538–546, 1991.
- [40] M. R. Gruber, N. L. Messersmith, and J. C. Dutton. Three-dimensional velocity field in a compressible mixing layer. *AIAA Journal*, 31(11):2061–2067, 1993.